

# Colossal Cryogenic Electro-Optic Response Through Metastability in Strained BaTiO<sub>3</sub> Thin Films

Albert Suceava, Sankalpa Hazra, Aiden Ross, Ian Reed Philippi, Dylan Sotir, Brynn Brower, Lei Ding, Yingxin Zhu, Zhiyu Zhang, Himirkanti Sarker, Saugata Sarker, Yang Yang, Suchismita Sarker, Vladimir A. Stoica, Darrell G. Schlom, Long-Qing Chen, and Venkatraman Gopalan\*

The search for thin film electro-optic materials that can retain superior performance under cryogenic conditions has become critical for quantum computing. Barium titanate thin films show large linear electro-optic coefficients in the tetragonal phase at room temperature, which is severely degraded down to  $\approx 200 \text{ pm V}^{-1}$  in the rhombohedral phase at cryogenic temperatures. There is immense interest in manipulating these phase transformations and retaining superior electro-optic properties down to liquid helium temperature. Utilizing the thermodynamic theory of optical properties, a large low-temperature electro-optic response is designed by engineering the energetic competition between different ferroelectric phases, leading to a low-symmetry monoclinic phase with a massive electro-optic response. The existence of this phase is demonstrated in a strain-tuned BaTiO<sub>3</sub> thin film that exhibits a linear electro-optic coefficient of  $2516 \pm 100 \text{ pm V}^{-1}$  at 5 K, which is an order of magnitude higher than the best reported performance thus far. Importantly, the electro-optic coefficient increases by  $100 \times$  during cooling, unlike the conventional films, where it degrades. Further, at the lowest temperature, significant higher order electro-optic responses also emerge. These results represent a new framework for designing materials with property enhancements by stabilizing highly tunable metastable phases with strain.

## 1. Introduction

The electro-optic (EO) effect in lithium niobate crystals enables our internet by encoding electrical to optical signals.<sup>[1–3]</sup> The EO effect describes the change in refractive index,  $n$ , of a material due to an applied electric field,  $E_k$ , given by  $\Delta \left(\frac{1}{n^2}\right)_{ij} = r_{ijk} E_k + s_{ijkl} E_k E_l$  in nonmagnetic materials, where  $r_{ijk}$  is the Pockel tensor representing the linear effect,  $s_{ijkl}$  is the Kerr tensor representing the quadratic effect, and the dummy subscripts indicate crystal physics axes. This allows for the phase, amplitude, or polarization of light to be modulated by a driving electrical signal. Electro-optic materials have recently re-emerged as a key technology in the field of quantum computing, where the EO effect can be leveraged to perform microwave-to-optical transduction.<sup>[4,5]</sup> Qubits based on Josephson junctions and trapped ions utilize microwave frequencies to write and read quantum states at cryogenic temperatures.<sup>[6–9]</sup> Electro-optic

A. Suceava, S. Hazra, A. Ross, H. Sarker, S. Sarker, V. A. Stoica, L.-Q. Chen, V. Gopalan  
 Department of Materials Science and Engineering  
 The Pennsylvania State University  
 University Park, PA 16802, USA  
 E-mail: [vgopalan@psu.edu](mailto:vgopalan@psu.edu)  
 I. R. Philippi, B. Brower, V. Gopalan  
 Department of Physics  
 The Pennsylvania State University  
 University Park, PA 16802, USA

D. Sotir  
 Platform for the Accelerated Realization, Analysis, and Discovery of Interface Materials (PARADIM)  
 Cornell University  
 Ithaca, NY 14853, USA  
 D. Sotir, D. G. Schlom  
 Department of Materials Science and Engineering  
 Cornell University  
 Ithaca, NY 14853, USA  
 L. Ding, Y. Zhu, Z. Zhang, Y. Yang  
 Department of Engineering Science and Mechanics  
 The Pennsylvania State University  
 University Park, PA 16802, USA  
 S. Sarker  
 Cornell High Energy Synchrotron Source  
 Cornell University  
 Ithaca, NY 14853, USA

 The ORCID identification number(s) for the author(s) of this article can be found under <https://doi.org/10.1002/adma.202507564>

© 2025 The Author(s). Advanced Materials published by Wiley-VCH GmbH. This is an open access article under the terms of the [Creative Commons Attribution](https://creativecommons.org/licenses/by/4.0/) License, which permits use, distribution and reproduction in any medium, provided the original work is properly cited.

DOI: 10.1002/adma.202507564

materials are required for the transduction of these microwave signals (operating at millikelvin temperature) to communicate with infrared light that is the standard for optical networks (operating at room temperature). Cryogenic electro-optics is also important for on-chip quantum photonic circuits, trapped ion quantum computing schemes, and developments in low-temperature science.<sup>[5,10–14]</sup> Nonetheless, a materials gap exists, namely EO materials operating at cryogenic temperatures with low thermal budget and a small footprint directly integrated on a chip and with electro-optic coefficients of  $r_{\text{eff}} > 1000 \text{ pm V}^{-1}$ . No such materials currently exist. Barium titanate ( $\text{BaTiO}_3$ ) appears promising because of its large  $r_{51} \approx 1640 \text{ pm V}^{-1}$  at room temperature; however the best literature reported value for films of  $\text{BaTiO}_3$  is  $r_{\text{eff}} \approx 200 \text{ pm V}^{-1}$  at 4 K.<sup>[14,15]</sup> In these prior studies, the temperature-dependent performance of the device revealed a nearly  $3 \times$  reduction in  $r_{\text{eff}}$  following cooling from room to cryogenic temperature, owing to the occurrence of multiple ferroelectric–ferroelectric phase transitions. Attempts to suppress or overcome these transitions have not yielded significant improvements thus far. With regards to its electrical properties, the microwave dielectric properties of  $\text{BaTiO}_3$  ceramics prepared under various methods have been extensively characterized, with the dielectric function generally rolling off above 10 GHz with an accompanying increase in loss.<sup>[16–23]</sup> Regardless, existing examples of electro-optic modulators based on thin film  $\text{BaTiO}_3$  have promisingly demonstrated a consistent response at cryogenic temperatures under modulation frequencies up to 30 GHz, leaving the low-temperature functional optical properties as a significant area for improvement.<sup>[14]</sup>

Many high-performance piezoelectric materials are discovered at morphotropic phase boundaries, namely regions where compositional tuning forces a competition between distinct structural phases, yielding an intermediate low symmetry phase with superior properties relative to the parents.<sup>[24–28]</sup> Similarly, across thermotropic phase boundaries in  $\text{BaTiO}_3$  and  $\text{KNbO}_3$  single crystals, low symmetry monoclinic phases are stabilized by local strain and fields generated within frustrated domain microstructures created by cycling across thermal phase transitions.<sup>[29]</sup> In particular, the optical second harmonic generation coefficients in  $\text{BaTiO}_3$  single crystals were enhanced by up to  $4.4 \times$  relative to the bulk values, and by  $2.3 \times$  in  $\text{KNbO}_3$  in metastable monoclinic phases stabilized by inhomogeneous strain and fields. One strategy to engineer large nonlinear optical property enhancements is

thus to stabilize metastable phases, but homogeneously over the entire sample.

We demonstrate this in  $\text{BaTiO}_3$  thin films, a material recognized for having one of the largest electro-optic coefficients in its tetragonal (T) phase at room temperature in its bulk form and thus being at the forefront of the search for cryogenic electro-optic materials.<sup>[15,30–32]</sup> Using phase-field simulations, we design the optimal epitaxial strain conditions to promote the competition between ferroelectric phases near liquid helium temperatures, resulting in a cryogenic monoclinic (M) phase. The films demonstrate a  $10 \times$  improvement in the electro-optic effect over the best demonstrated values in the literature at 10 K.<sup>[14]</sup> Our findings demonstrate a new paradigm for engineering electro-optic materials under cryogenic conditions.

## 2. Temperature-Strain Phase Diagram of $\text{BaTiO}_3$

Bulk  $\text{BaTiO}_3$  undergoes a series of phase transitions from cubic to tetragonal at 130 °C, tetragonal to orthorhombic at 5 °C, and orthorhombic to rhombohedral at –90 °C.<sup>[33,34]</sup> **Figure 1a** depicts the predicted temperature-dependent phase diagram of  $\text{BaTiO}_3$  as a function of biaxial epitaxial strain,  $\epsilon = (a_{\parallel} - a_o)/a_o$ , where  $a_o$  is the equivalent cubic lattice parameter extrapolated from the high temperature  $\text{BaTiO}_3$  cubic phase (4.008 Å) and  $a_{\parallel}$  is the in-plane lattice parameter of the biaxially strained  $\text{BaTiO}_3$ . Under a biaxial compressive strain, the tetragonal  $c$  (space group  $P4mm$ ) phase becomes more stable by minimizing its elastic energy as compared to the other ferroelectric phases. As the biaxial compressive strain decreases, an energetic competition between the chemical energy, which determines the intrinsic stability of the ferroelectric phases (favoring the rhombohedral phase at low temperatures), and the elastic energy (favoring the tetragonal  $c$  phase) emerges. Under certain strain conditions at cryogenic temperatures, this competition results in a compromise between the two energetic components resulting in the monoclinic  $a$  ( $M_a$ ) phase (space group  $Cm$ ), which is a bridging phase between the tetragonal and rhombohedral phase.<sup>[35]</sup> In addition to the thermodynamically stable phases, after applying an electric field and retracting we find that there exists a field-induced metastable monoclinic phase that extends beyond the equilibrium monoclinic phase boundary, forming a monoclinic  $c$  phase ( $M_c$ ) (space group  $Pm$ ), which acts as a bridging phase between the tetragonal and orthorhombic phase, as depicted in **Figure 1b**.

As the temperature decreases further, the system approaches the tetragonal (T) to monoclinic (M) phase boundary, where these competing phases are nearly degenerate in energy. In this regime, a small electric field can shift the thermodynamic stability between states inducing a polarization rotation and enabling a large electro-optic response, as depicted in **Figure 1c**. By integrating the thermodynamic theory of optical properties in ferroelectrics with phase-field simulations, we compute the temperature-dependent electro-optic response at 1550 nm.<sup>[36]</sup> Our results predict a large enhancement of the linear electro-optic coefficient, driven by the highly susceptible ferroelectric polarization of the monoclinic phase near the phase boundary. The

Y. Yang  
Department of Nuclear Engineering  
The Pennsylvania State University  
University Park, PA 16802, USA

Y. Yang  
Materials Research Institute  
The Pennsylvania State University  
University Park, PA 16802, USA

D. G. Schlom  
Kavli Institute at Cornell for Nanoscale Science  
Ithaca, NY 14853, USA

D. G. Schlom  
Leibniz-Institut für Kristallzüchtung  
Max-Born-Straße 2, 12489 Berlin, Germany

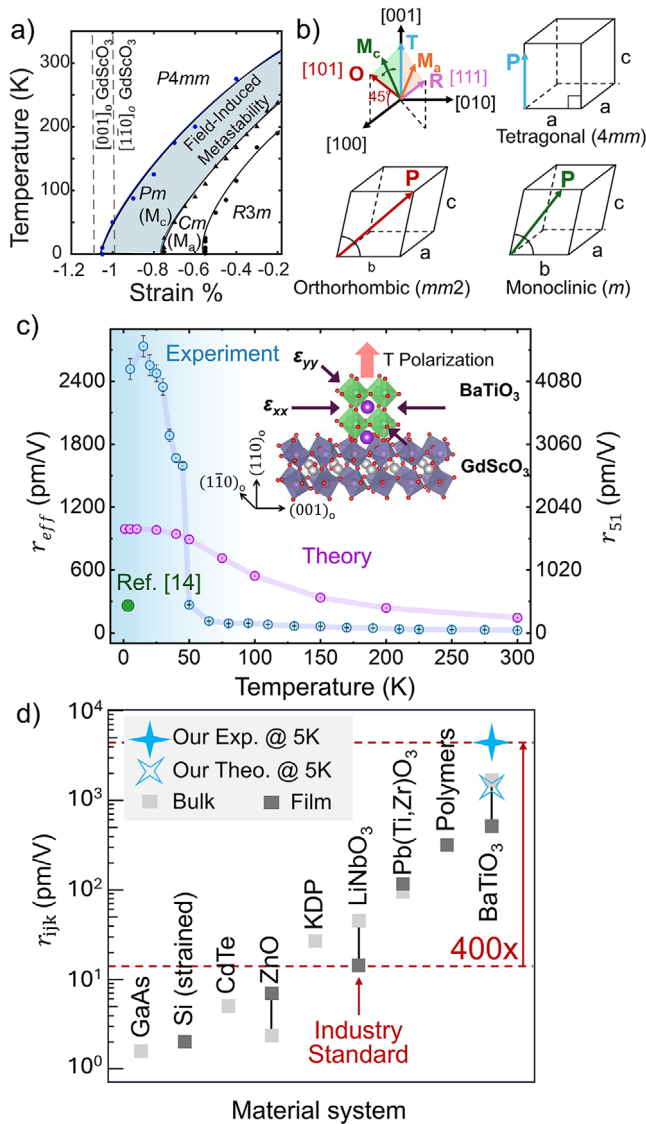


**Figure 1.** a) Temperature-strain phase diagram for compressively strained BaTiO<sub>3</sub> from phase-field simulations. The blue region indicates a metastable monoclinic phase that may be created by applying an electric field perpendicular to the tetragonal axis and removing it subsequently. b) Representation of polarization directions in tetragonal, orthorhombic, and intermediate monoclinic phases. c) Comparison between experimentally measured (blue) and phase-field simulation (purple) curves of the effective electro-optic coefficient responsible for the index change observed under the experimental geometry of Figure 2a. Comparison to the leading cryogenic coefficient found in literature is provided in (green).<sup>[14]</sup> (inset) Schematic of epitaxial BaTiO<sub>3</sub> under a compressive biaxial strain. d) Comparison between the maximum electro-optic response obtained in this work and several other benchmark materials.

general behavior may be understood using the thermodynamic theory of the electro-optic effect:

$$r_{131} = \left( \frac{\partial B_{13}}{\partial E_1} \right) \cong \left( \frac{\partial B_{13}}{\partial P_1^L} \right) \left( \frac{\partial P_1^L}{\partial E_1} \right) = f_{131}^L \chi_{11}^L \quad (1)$$

where  $r_{ijk}$  is the electro-optic coefficient,  $B_{ij} = \left( \frac{1}{n^2} \right)_{ij}$  is the optical dielectric stiffness defined in terms of the refractive index  $n$ ,  $P_i^L$  is the lattice polarization (the ionic and electronic components of ferroelectric polarization, which arises due to the displacement of the lattice), and  $E_i$  is the electric field. We decompose the electro-optic coefficient into a linear polar-optic effect ( $f_{131}^L$ ) and the dielectric susceptibility of the lattice polarization ( $\chi_{11}^L$ ). The linear polar-optic effect is proportional to the spontaneous polarization and remains roughly constant down to low temperature in the compressively strained films. Therefore, the enhancement of the electro-optic effect is primarily driven by the increase of  $\chi_{11}^L$  near the tetragonal-to-monoclinic phase boundary, where the lattice polarization is highly susceptible to rotation within the monoclinic mirror plane  $m$ .

### 3. The Electro-Optic Effect in Strained BaTiO<sub>3</sub>

#### 3.1. Cryogenic Electro-Optic Response

To validate this design approach, we characterize the magnitude of the Pockels effect in BaTiO<sub>3</sub> grown on (110)<sub>o</sub> GdScO<sub>3</sub> (subscript “o” for orthorhombic), where lattice mismatch results in a compressive strain of  $-1.0\%$ . Epitaxial growth of a  $\approx 37$  nm film was achieved by using molecular-beam epitaxy with in-situ reflection high-energy electron diffraction (RHEED) to monitor surface quality. As shown in Figures S1 and S2 (Supporting Information), asymmetric reciprocal space maps taken at the GdScO<sub>3</sub> 332<sub>o</sub> peak reveal alignment with the BaTiO<sub>3</sub> 103<sub>t</sub> (subscript “t” for tetragonal) peak in  $Q_x$ , confirming epitaxial growth.  $\theta$ -2 $\theta$  X-ray diffraction scans confirm  $c$ -axis out-of-plane orientation of the films in the room temperature T phase, with rocking curve measurements demonstrating film peaks with full-width half-max measures of 119 arcsec as shown in Figure S3 (Supporting Information). Post growth atomic force microscope scans reveal a root-mean-squared surface roughness of 392 pm as shown in Figure S4 (Supporting Information), confirming a smooth film morphology. Piezoelectric force microscopy scans shown in Figure S5 (Supporting Information) failed to provide evidence for antipolar domain structures. High-resolution scanning transmission electron microscopy images confirm coherent epitaxial growth and high interfacial quality, as shown in Figure S6 (Supporting Information). Additional experimental details on film growth and structural characterization are provided in Section 5.

Due to the compressive strain enforced by the substrate, at room temperature, the BaTiO<sub>3</sub> films are entirely tetragonal with the polar [001] axis in the out-of-plane direction. 500 nm square electrodes of 80 nm Pt/5 nm Ti were lithographically deposited onto the film surface with a separation gap of 200  $\mu$ m to apply a field in the in-plane direction, corresponding to the [100] crystallographic direction, with a schematic of this shown in Figures S7 and S8 (Supporting Information). In the T phase of BaTiO<sub>3</sub>, the crystal physics 1, 2, and 3 directions are conveniently aligned with the crystallographic [100], [010], and [001] directions.

Electro-optic measurements were performed using a polarizer-sample-compensator-analyzer (PSCA) based measurement setup, as shown in Figure 2a.<sup>[37–52]</sup> In this method, the change

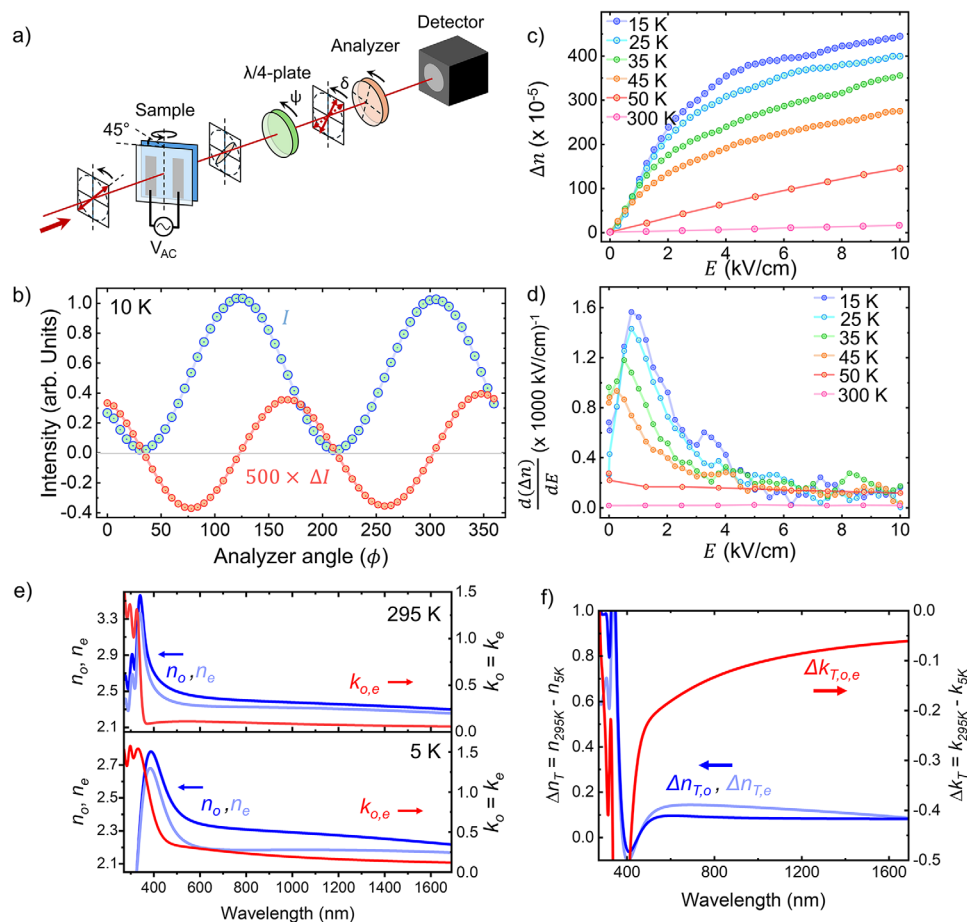


**Figure 2.** a) Schematic of experimental PCSA setup for measuring the electro-optic coefficient. b) Experimental unmodulated and modulated intensity curves, displaying the expected  $\pi/2$  relative phase shift. c)  $\Delta n$  versus applied electric field taken at the analyzer angle which maximizes the modulated intensity at different temperatures. d) The derivative of  $\Delta n$  versus applied electric field curves, showing the offset bias required for maximum modulation efficiency. e) Refractive index and extinction coefficient of strained BaTiO<sub>3</sub> film versus wavelength, at room temperature and at 5 K, as determined by variable angle ellipsometry. f) Relative refractive index and extinction coefficient changes between room temperature and 5 K,  $\Delta n_T = n_{295K} - n_{5K}$ ,  $\Delta k = k_{295K} - k_{5K}$ .

in transmission of light through a pair of crossed polarizers as a function of applied electric field is detected to quantify the change in the refractive indices of the sample. Further details on the operating principle are provided in Section 4 and within ref. [37–52]. A knife-edge characterization of the probe beam is provided in Figure S9 (Supporting Information). Other measurement methods, such as the Teng–Man approach, were considered, but the PCSA method ultimately pursued due to the restrictions the epitaxial strain condition imposes on the electrode geometry. Confidence in the measurement procedure was established by determining the electro-optic coefficient of a well-known LiNbO<sub>3</sub> reference sample, whose data are included in Figure S10 (Supporting Information).

For characterization of the BaTiO<sub>3</sub> on GdScO<sub>3</sub> sample of interest, the incident polarization is set to lie between two principal optic axes of the sample, which in this study are the [100] and [010] in-plane crystallographic axes of the BaTiO<sub>3</sub> film. The BaTiO<sub>3</sub> thin film refractive indices were characterized using spectroscopic ellipsometry at room temperature and at 5 K. The extracted dispersion curves are shown in Figure 2e, and a detailed

description of the optical modeling procedure and additional reflection and transmittance measurements performed is provided in Note S3, Figures S11 and S12 (Supporting Information). The ellipsometry measurements also served to refine the film thickness to a value of 36.53 nm, which was used in the subsequent analysis. With an in-plane electric field  $E_1$ , the index ellipsoid of the tetragonal phase distorts following Equation (2), taking the original 1, 2, and 3 principal axes to a new set of axes: 1', 2' = 2, 3':

$$\frac{x^2}{n_1^2} + \frac{y^2}{n_2^2} + \frac{z^2}{n_3^2} + 2xz r_{51} E_1 = 1 \quad (2)$$

In the absence of the field  $E_1$ ,  $x \equiv 1$ ,  $y \equiv 2$ ,  $z \equiv 3$  are the principal (Eigen) crystal physics axes, and  $n_1$ ,  $n_2$ ,  $n_3$  are the principal refractive indices along those directions with  $n_1 = n_2 = n_o$  and  $n_3 = n_e$  for the T phase of BaTiO<sub>3</sub>, a negative uniaxial material.<sup>[1]</sup> The action of  $r_{51}$  (the last term in Equation (2)) would lead to new Eigen coordinates in the  $x$ - $z$  plane, leading to  $x' \equiv 1'$  and  $z' \equiv 3'$  axes. The  $y' \equiv 2' = y \equiv 2$  would remain unchanged under this

field. This point is illustrated in detail in Note S4 and Figure S15 (Supporting Information).

To detect the electro-optic effect under this geometry, where the  $z \equiv 3$  axis is pointed normal to the film surface, the sample was tilted  $45^\circ$  away from the incident probe as depicted in Figure 2a. This results in the probe beam now experiencing two orthogonal refractive indices  $n_o$  and  $n_e(\theta)$  without any external voltage applied to the sample, and  $n'_o = n_o$  and  $n'_e(\theta)$  with the voltage applied. The birefringence induced by the sample results in a change in the probe polarization from a linear to an elliptical state, resulting in a non-zero transmission through an analyzer oriented orthogonally to the initial polarization state when a voltage is applied.

The unmodulated transmission function,  $I$ , of this system without an applied electric field is described  $I = I_0 \cos^2(\phi + \delta)$ , where,  $\phi$  represents the angle through which the analyzer is rotated and  $\delta$  represents an overall phase angle accumulated during beam transmission through the sample and other optical components before the analyzer, as shown in Figure 2a. When an applied electric field is applied across the sample, the resulting modulation to the transmission function,  $\Delta I$ , can be expressed with respect to the first order in  $\Delta\delta$  as follows:

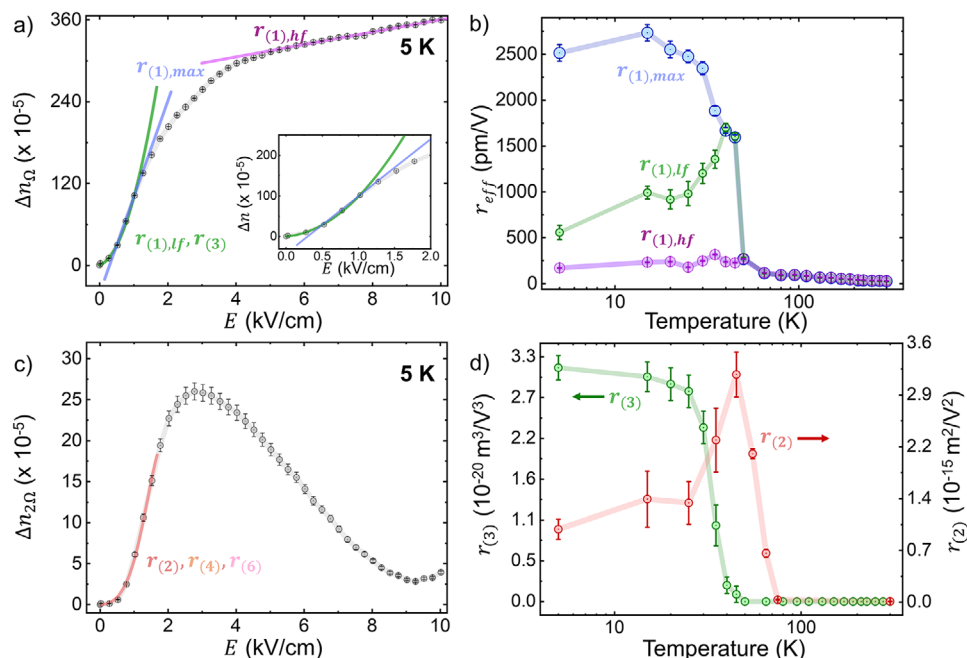
$$\Delta I = I_0 \Delta\delta \sin 2(\phi + \delta) \quad (3)$$

Figure 2b shows the experimentally measured  $I$  and  $\Delta I$  curves at 10 K for the BaTiO<sub>3</sub> on GdScO<sub>3</sub> sample fitted to the above equations. The derived  $\Delta\delta$  can be converted into the electric-field induced birefringence,  $\Delta n = \frac{\Delta\delta\lambda}{2\pi L}$ , where,  $\lambda = 1550$  nm is the wavelength of light used for measurements, and  $L$  is the distance light travelled through the BaTiO<sub>3</sub> film given by  $L = t/\cos \theta_{\text{film}}$ , where  $t$  is the film thickness and  $\theta_{\text{film}}$  is the angle describing the direction of propagation of light inside the film layer, considering the  $45^\circ$  probe angle of incidence and Snell's law and assuming a single pass. The effective electro-optic coefficient,  $r_{\text{eff}} = \frac{2\Delta n}{n_e(\theta_{\text{film}})^3 E}$  is then calculated, where  $E$  is the amplitude of the AC bias applied to the sample to measure the modulated transmission function,  $\Delta I$  and  $n_e(\theta_{\text{film}})$  is the refractive index seen by p-polarized light, described at length in Note S4 (Supporting Information). Following Equation (3), the experimentally measured maximum value for the modulated transmission function,  $\Delta I$ , is obtained at the analyzer angle that results in the halfway point of the unmodulated transmission function,  $I$ , which is where the slope is maximized resulting in a  $\frac{\pi}{2}$  phase shift between the two curves. A linear dependence in the maximum modulated intensity plotted against the applied electric field above 50 K (Figure 2c), confirms the origin of the response as the Pockels effect. The nonlinear behavior that emerges below 50 K is discussed in the following sections. This measurement is performed at several discrete temperatures to characterize the low-temperature properties of the sample, with the compensator position,  $\psi$ , optimized to cancel out the native birefringence of the sample at every temperature. The effective electro-optic coefficient observed,  $r_{\text{eff}}$ , is converted into the tensor coefficient  $r_{51}$  through a geometrical analysis of the modulated index ellipsoid, as described in Note S4 (Supporting Information).

The unmodulated refractive index was directly measured at room temperature and at 5 K. For the analysis described in the

preceding section, the refractive index measured at 5 K was used to analyze electro-optic data collected below 50 K, while the room temperature index was used to interpret data collected above 50 K. The separation between data sets at 50 K is chosen to reflect the phase transition that occurs at that temperature, as seen in the electro-optic measurements and second harmonic generation data to follow. An analysis of the electro-optic response using a linear interpolation of these refractive index values as opposed to a step function is presented in Figure S14 (Supporting Information). With the effective electro-optic coefficient expressed in full as  $r_{\text{eff}} = \frac{2}{n_e(\theta_{\text{film}})^3 E} \left( \frac{\Delta I \cdot \lambda}{I_0 \cdot 2\pi L} \right)$ , the collective error can be expressed as the sum of the errors of all terms in the products weighed by their exponents:  $\frac{dr_{\text{eff}}}{r_{\text{eff}}} = 3\left(\frac{dn_o}{n_o}\right) + \frac{dE}{E} + \frac{d\Delta I}{\Delta I} + \frac{dI_0}{I_0} + \frac{dL}{L}$ . In other words, every percent error in the unmodulated refractive index will propagate a three times larger percent error in the extracted electro-optic coefficient. Assuming that the refractive index in the temperature range between 5 and 295 K lies between the two endpoints measured, this results in a maximum error in the index equal to the difference between the two values, which is an error of 3.4%. Thus, the maximum error in the determination of the electro-optic coefficients due to inaccuracy in the index interpolation becomes 10.2%. An increase in the extinction coefficient of the film at low temperature may arise from the transition from a unipolar tetragonal structure to a multidomain monoclinic structure with potentially four domain variants, which might promote additional scattering of light from the domain walls.<sup>[53,54]</sup>

As shown in Figure 1c, the measured effective electro-optic coefficient reaches a peak value of  $2735 \pm 100$  pm V<sup>-1</sup> at a temperature of 15 K, representing over a  $100 \times$  enhancement from the room temperature value of  $25 \pm 2$  pm V<sup>-1</sup>. This is in direct contrast with previous results in the literature, where the electro-optic coefficients of relaxed BaTiO<sub>3</sub> films are reduced to nearly a third of their room temperature value at similar temperatures.<sup>[14]</sup> It is important to acknowledge that the room temperature electro-optic coefficient of the strained BaTiO<sub>3</sub> is lower than that of relaxed films grown on Si found in literature.<sup>[31]</sup> Phase-field simulations provide support for this trade-off being an intrinsic effect of the strained condition. There also exists the possibility of the grown film possessing oppositely oriented tetragonal  $c$  domains resulting in a reduction in the observed electro-optic effect. Piezoelectric force microscopy was performed to image such potential antipolar domains, but no such domains were revealed, Figure S5 (Supporting Information). Nevertheless, the strained condition leads to superior performance at low temperatures. The reproducibility of this response is discussed in Note S5, Figure S17, and Table S3 (Supporting Information) with regards to both thermal and electrical cycling. While the sample appears to be remarkably robust and consistent with regards to electrical cycling, some variation in the nonlinear response is observed in every instance the sample is cooled. Most noteworthy is a reduction in the largest observed  $r_{\text{eff}}$  after the sample had undergone several cooling-heating cycles, suggesting that thermal hysteresis and the initial configuration of the domain microstructure at low temperature carries significant implications for the nonlinear electro-optic response. The large enhancement at cryogenic temperatures arises from the emergence of the M<sub>c</sub> phase as discussed next.



**Figure 3.** a) Various interpretations of the effective electro-optic response  $r_{eff}$ , depending on which part of the nonlinear response is of interest. b)  $r_{(1),max}$ ,  $r_{(1),hf}$  and  $r_{(1),lf}$  as a function of temperature. c) Observed electro-optic response recorded at double the modulation frequency,  $2\Omega$ , as a function of temperature, indicating a nonlinear response d) Higher order electro-optic coefficients  $r_{(2)}$  and  $r_{(3)}$  extracted from polynomial fits of the nonlinear  $2\Omega$  and  $\Omega$  frequency responses, respectively.

### 3.2. Nonlinearity in the Cryogenic Electro-Optic Response

The field dependence of the electro-optic response exhibits a striking difference below 50 K from that above (Figure 2c), where a field-dependent nonlinearity is observed. Below 50 K, a knee in the curves becomes apparent, separating a linear regime at high fields from a much stronger linear response at low fields. Below 25 K, a second knee emerges at very low fields roughly below  $0.5 \text{ kV cm}^{-1}$ , resulting in an S-curve-like shape as shown in Figure 3a. Response curves of the predicted monoclinic phase can thus be discussed in terms of three different regimes: the low-field limit, where the index change appears strictly nonlinear, a mid-range high-slope linear regime containing the point of inflection for the curve, and a lower-slope high-field linear regime.

An examination of the derivative of  $\Delta n$  as a function of  $E$  curves (Figure 2d) reveals that the slope of the high-field regime converges to a common value, which corresponds to an  $r_{eff} = r_{(1),hf} \approx 200 \text{ pm V}^{-1}$ , the temperature dependence of which is displayed in Figure 3b. The derivative of  $\Delta n$  as a function of  $E$  also reveals the exact point of inflection of the response curves located in the intermediate voltage range, where the magnitude of the linear electro-optic response is maximized. By taking the linear slope at the inflection point, one can define a second value for  $r_{eff} = r_{(1),max}$ , depicted in Figure 3a. It is this value of  $r_{eff}$  that is presented in Figure 1c. From an engineering perspective,  $r_{(1),max}$  can be accessed by applying a small DC bias offset alongside AC modulation to maximize the sensitivity of the electro-optic response. This DC bias would be equivalent to the point where the derivative of  $\Delta n$  as a function of  $E$  is maximized, as shown in Figure 2d. For response curves below 35 K, the low field regime can be fit by a higher-order polynomial function in odd powers.

The choice to only attempt a fit with odd-order polynomial terms can be understood by considering the higher-order expansion of the electro-optic effect under an AC field:  $\Delta \left( \frac{1}{n(t)} \right)^2 = \sum_n r_{(n)} E(t)^n$  where  $(n)$  denotes the  $n^{\text{th}}$  order electro-optic effect ( $r_{(n)}$  is not to be confused with  $r_{ij}$  the linear electro-optic tensor coefficient). For a sinusoidal field the electro-optic response becomes:  $-\Delta n(t) \frac{2}{n^3} = \sum_n r_{(n)} E_0^n \cos^n(\Omega t)$ , where  $\cos^n(\Omega t)$  can be expanded as:

$$\cos^n(\Omega t) = \frac{1}{2^{n-1}} \sum_{k=\frac{n}{2}+1}^n \binom{n}{k} \cos[(2k-n)\Omega t] + \frac{1}{2^n} \binom{n}{n/2} \text{ for even } n \quad (4)$$

$$\cos^n(\Omega t) = \frac{1}{2^{n-1}} \sum_{k=\frac{n}{2}+1}^n \binom{n}{k} \cos[(2k-n)\Omega t] \text{ for odd } n \quad (5)$$

It follows then that:

$$\begin{aligned} -\Delta n(t) \frac{2}{n^3} = & \left( \frac{1}{2} r_{(2)} E_0^2 + \frac{3}{8} r_{(4)} E_0^4 + \frac{5}{16} r_{(6)} E_0^6 + \dots \right) \\ & + \left( r_{(1)} E_0 + \frac{3}{4} r_{(3)} E_0^3 + \frac{5}{8} r_{(5)} E_0^5 + \dots \right) \cos(\Omega t) \\ & + \left( \frac{1}{2} r_{(2)} E_0^2 + \frac{1}{2} r_{(4)} E_0^4 + \frac{15}{32} r_{(6)} E_0^6 + \dots \right) \cos(2\Omega t) \\ & + \left( \frac{1}{4} r_{(3)} E_0^3 + \frac{5}{16} r_{(5)} E_0^5 + \dots \right) \cos(3\Omega t) \\ & + \left( \frac{1}{8} r_{(4)} E_0^4 + \frac{3}{16} r_{(6)} E_0^6 + \dots \right) \cos(4\Omega t) \end{aligned} \quad (6)$$

It can be seen then that when detecting an electro-optic response at the same frequency as the driving field, only odd-powered higher order terms should manifest in the observed signal as experimentally detected by a lock-in amplifier.

A fit of up to third-order terms is sufficient for the low field regime of the electro-optic response recorded at the first harmonic of the driving electric field, with the resultant third-order electro-optic coefficients  $r_{(3)}$  shown as a function of temperature in Figure 3d. Equation (6) also reveals that an intrinsically nonlinear material response is expected to yield a signal at detection frequencies that are higher harmonics of the driving electric field. Specifically, the presence of a quadratic electro-optic effect should be detected when locking on to twice the modulation frequency and integer multiples thereof. In order to confirm the nonlinear nature of the material response at cryogenic temperatures,  $\Delta n$  versus  $E$  curves were also measured at several discrete temperatures while locking on to double the frequency of the modulation field,  $2\Omega$ , with a representative result shown in Figure 3c and curves obtained at other temperatures shown in Figure S18b (Supporting Information). A fit of up to 6th order terms yields very good agreement with the data at low fields. We note that to fit the response curve for the full range of voltages applied, yet even higher order terms are required. The extracted quadratic electro-optic coefficients  $r_{(2)}$  are provided in Figure 3d, while the temperature dependence of the higher order terms  $r_{(4)}$  and  $r_{(6)}$  is provided in Figure S18a (Supporting Information). A phenomenological model based on the Avrami equation is also capable of providing an approximate fit to the nonlinear response, as shown in Figure S19 (Supporting Information). This model is further discussed in Note S6 (Supporting Information).

Comparing different methods of defining the linear  $r_{\text{eff}}$  as  $r_{(1),\text{max}}$ ,  $r_{(1),\text{hf}}$ , and  $r_{(1),\text{lf}}$  reveals a convergence above 50 K when the nonlinearity in the response curves vanishes. The  $r_{(1),\text{lf}}$  converges to  $r_{(1),\text{max}}$  with increasing temperature, while at low temperatures it approaches  $r_{(1),\text{hf}}$ , suggesting that as the S-curve character grows more prominent, the low-field regime may mirror the high-field regime. The relationship between the Pockels  $r_{\text{eff}}$  and individual tensor elements are discussed in detail in Note S4 (Supporting Information), which includes a discussion on all possible tensor element contributions to the observed response and experiments conducted in an attempt to isolate the dominant coefficients. Following these considerations and supported by phase field simulations shown in Figure S16 (Supporting Information), the  $r_{\text{eff}}$  is found to primarily reflect the intrinsic  $r_{51}$  Pockels coefficient reduced by a factor of  $\approx 1.7 \times$ , yielding a maximum value of  $r_{51} = 4649 \pm 170 \text{ pm V}^{-1}$  at 15 K, as shown in Figure 1c.

The quadratic response observed at  $2 \Omega$  is found to maximize  $\approx 50 \text{ K}$  where the nonlinear response initially sets in. The fitted response is found to be within the same order of magnitude as  $s_{11} - s_{12} = r_{(2),11} - r_{(2),12}$  measures of the observed quadratic electro-optic effect in bulk  $\text{BaTiO}_3$  ( $s_{ij}$  being the more common notation for the quadratic electro-optic effect as opposed to  $r_{(2),ij}$ ), and several orders of magnitude higher than the response of other classical nonlinear optical materials like  $\text{KH}_2\text{PO}_4$  (KDP).<sup>[1,55]</sup> We note that while the observed  $\Delta n_{2\Omega}$  continues to increase with decreasing temperature, this does not manifest as an increase in the extracted  $r_{(2)}$ , but rather in the higher order  $r_{(4)}$  and  $r_{(6)}$  terms required to yield a good fit of the complex response (Figure S18, Supporting Information). Further exploration of the full extent of this nonlinearity with regards to even higher harmonic responses and extraction of higher or-

der electro-optic coefficients will be investigated in subsequent works.

The nonlinearity, which is primarily responsible for the cryogenic property enhancement as defined through  $r_{(1),\text{max}}$  appears to be correlated to the emergence of the metastable monoclinic structure. For applied fields below the saturation regime, a continuous monoclinic distortion can be produced through a “swaying” of the ferroelectric polarization vector away from the tetragonal out-of-plane  $c$ -axis, with an in-plane component developing in the direction of the applied field. This results in a large lattice dielectric susceptibility and large electro-optic response. Nonetheless, polarization rotation eventually saturates near  $21^\circ$  (as predicted by phase-field simulation) and the lattice susceptibility is reduced leading to the high-field regime.<sup>[56]</sup>

### 3.3. Understanding the $M_c$ Phase Through Optical Second-Harmonic Generation

To confirm the presence of a new monoclinic phase below 50 K, complementary second-harmonic generation (SHG) polarimetry measurements were performed (see Section 5: Experimental Section). The SHG process describes the generation of light at frequency  $2\omega$  when light of frequency  $\omega$  passes through a non-centrosymmetric medium following the third-rank tensor equation:  $P_i^{2\omega} = \epsilon_0 d_{ijk} E_j^\omega E_k^\omega$ , where  $E_j^\omega$  and  $E_k^\omega$  are optical electric fields at frequency  $\omega$  and polarization directions  $j$  and  $k$ ,  $P_i^{2\omega}$  is the radiating nonlinear polarization generated in the material at frequency  $2\omega$  and polarization direction  $i$ , with efficiency described by the SHG tensor coefficient  $d_{ijk}$  of the material, and  $\epsilon_0$  the permittivity of vacuum.<sup>[2]</sup> Owing to its nature as a third-rank tensor property similar to the Pockels effect, polar phases and transitions can be observed with extreme sensitivity.<sup>[57]</sup> At normal incidence, no SHG was observed at room temperature as expected for the tetragonal  $4mm$  phase. The observation of a non-zero SHG signal in this geometry would explicitly confirm a reduction in symmetry of the film structure. Indeed, the normal incidence SHG (Figure 4b) is zero until 50 K, confirming a transition to a lower symmetry structure. This is consistent with the prediction of the in-plane ferroelectric polarization component,  $P_x$ , as a function of temperature (Figure 4a). SHG polarimetry performed at  $\theta = 45^\circ$  incidence (Figure 4c) and its modeling (see Note S7 and Table S4, Supporting Information) indicate a tetragonal  $4mm$  phase until 50 K followed by a monoclinic  $m$  structure with four domain variants arising from the positive and negative shear in each of the two mirror planes perpendicular to  $x$  and to  $y$ .<sup>[58]</sup> To further support the interpretation of the  $r_{(1),\text{max}}$  response as due to a monoclinic distortion under an external electric field, the electric-field-dependent SHG response is also measured and shown in Figure S20b–e (Supporting Information). Under an external field consistent with that applied during electro-optic experiments, the polarimetry curves continue to evolve in a way that requires a monoclinic  $m$  model to fit, suggesting that additional monoclinic distortions occur in the softened, low-temperature lattice. Hysteresis in the samples was observed by performing both electro-optic measurements under a DC bias and SHG measurements under DC bias. Both yield minimal discernible hysteretic behavior, with the results shown in

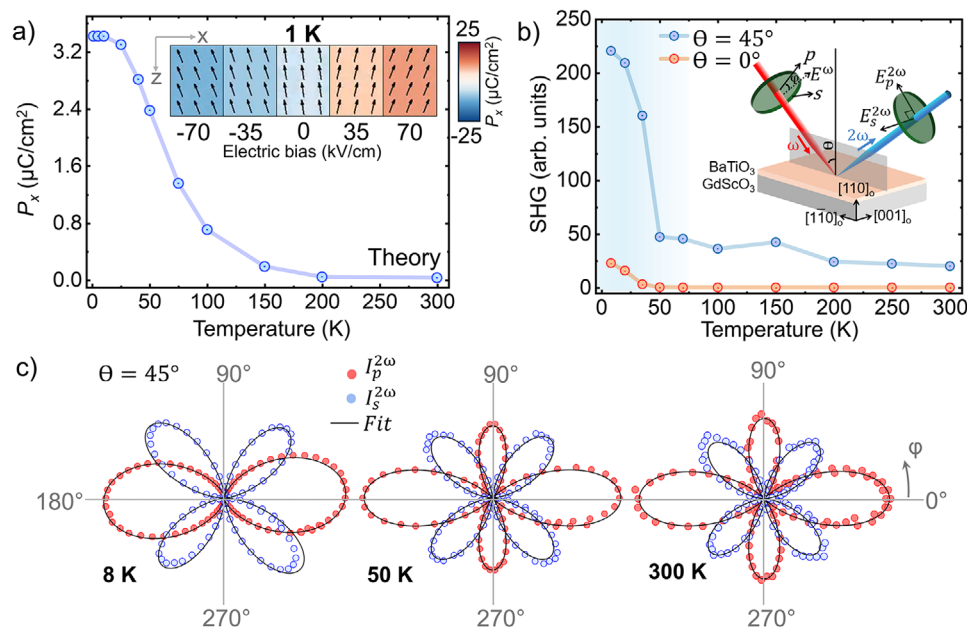


**Figure 4.** a) Phase-field simulated values of the in-plane polarization,  $P_x$ , as a function of temperature, reflecting the degree of monoclinic distortion. (inset) Phase field simulated polarization vectors under applied field at 1 K, showcasing the susceptibility of the lattice. b) SHG signal versus temperature at  $\theta = 0^\circ$  and  $\theta = 45^\circ$  incidence angle measurement conditions, for an input fundamental polarization,  $\varphi$ , along  $0^\circ$ . c) SHG polarimetry taken at  $\theta = 45^\circ$  incidence angle and at 300, 50, and 8 K, indicating tetragonal  $4mm$  symmetry at and above 50 K and a monoclinic  $m$  symmetry below 50 K. The solid lines are theory fits as described in Note S7 (Supporting Information).

Figure S21 (Supporting Information). These findings suggest that the metastable monoclinic phase enables a continuous, repeatable transformation of the polarization vector.

Additional low-temperature X-ray characterization could serve as explicit confirmation of the suspected cryogenic monoclinic phase and will be investigated in future work. Both SHG and X-ray characterization confirmed an analogous metastable phase in strained  $\text{KNbO}_3$  thin films, thus strengthening the SHG-based claims presented for  $\text{BaTiO}_3$ .<sup>[58]</sup>

## 4. Conclusion

Through theory and experiments, we demonstrate that strain can be used to engineer intermediate low-symmetry phases in  $\text{BaTiO}_3$  thin films, where a cryogenic metastable monoclinic phase exhibits a large linear electro-optic response, as well as a large nonlinear EO response. Due to the competition between multiple ferroelectric phases with similar thermodynamic stability, an emergent low-symmetry phase can be stabilized. This “bridging phase” manifests as a monoclinic structure, which is noteworthy for the ability of its lattice to deform in the presence of an applied electric field. The freedom for the polar axes to sway away from the tetragonal  $[001]$   $c$ -axis with an in-plane component in the  $(001)$  plane results in a large dielectric susceptibility and a large effective electro-optic effect, the highest reported thus far. Future work is required to measure this EO response at GHz frequencies where it is of technological importance. Nonetheless, this work illustrates the power of symmetry breaking and stabilizing new metastable states in thin films toward achieving superior properties that are otherwise not available in the equilibrium phases.

## 5. Experimental Section

**Growth of  $\text{BaTiO}_3$  on  $\text{GdScO}_3$  Thin Films:** The sample was grown in a Veeco GEN10 MBE system equipped with an epi-ray GmbH THERMALAS laser substrate heater, a 1 kW  $\text{CO}_2$  laser with a wavelength of  $10.6 \mu\text{m}$  that irradiates the backside of the substrate over a circular area with a diameter of  $\approx 14 \text{ mm}$ . Barium (Sigma-Aldrich, 99.99% purity) was supplied using a conventional differentially pumped effusion cell, and titanium using a Veeco Ti-Ball source. One monolayer of BaO was deposited first, after which the sources were simply co-deposited. The barium flux was  $\approx 5 \times 10^{13} \text{ atoms (cm}^2 \times \text{s)}^{-1}$  and the titanium flux was  $\approx 1 \times 10^{13} \text{ atoms (cm}^2 \times \text{s)}^{-1}$ , i.e., a Ba:Ti flux ratio of 5:1. The barium flux was determined by a quartz crystal microbalance, and the titanium flux by X-ray reflectivity of a calibration film of  $\text{BaTiO}_3$  grown on a  $\text{SrTiO}_3$   $(001)$  substrate at  $T_{\text{sub}} = 1200^\circ\text{C}$ , with an oxidant pressure of  $1 \times 10^{-6} \text{ Torr}$  of  $\text{O}_2 + 10\% \text{ O}_3$  and a Ba:Ti ratio of 5:1. The  $\text{BaTiO}_3$  film was grown on a  $\text{GdScO}_3$   $(110)_o$  substrate (CrysTec GmbH), to a thickness of  $\approx 36 \text{ nm}$ .

Ozone was used as the oxidant at a background pressure of  $1 \times 10^{-6} \text{ Torr}$  of  $\text{O}_2 + 10\% \text{ O}_3$ . The film was cooled in the same oxidant and pressure in which it was grown to  $T_{\text{sub}} < 200^\circ\text{C}$  before the oxidant was turned off. The substrate temperature, measured by a pyrometer operating at  $7.5 \mu\text{m}$  on the backside of the substrate during growth, was  $1160^\circ\text{C}$ . Due to the high substrate temperature, the vapor pressure of barium-containing species over  $\text{BaTiO}_3$ , chiefly BaO, was significantly higher than that of titanium-containing species over  $\text{BaTiO}_3$ , so excess barium will desorb from the surface leaving behind a single-phase  $\text{BaTiO}_3$  film within an adsorption-controlled growth window. As  $\text{GdScO}_3$  absorbs well at  $10.6 \mu\text{m}$ , the backside of the substrate was not coated.

X-ray diffraction (XRD) and reciprocal space mapping (RSM) analysis were done with a Panalytical Empyrean X-ray diffractometer using  $\text{Cu } K_{\alpha 1}$  radiation. Atomic force microscopy (AFM) was performed using an Asylum Cypher ES Environmental AFM. RHEED images were taken during growth using a Staib electron source operating at 14 kV.

**High Resolution Scanning Transmission Electron Microscopy:** A sample of the  $\text{BaTiO}_3$  on  $\text{GdScO}_3$  film was prepared for high-resolution scanning

transmission electron microscopy (HR-STEM) using focused ion beam (FIB) lift-out, followed by sequential milling at 30, 16, 5 kV, and a final cleaning at 2 kV to progressively reduce surface damage. Scanning transmission electron microscopy (STEM) and energy-dispersive X-ray spectroscopy (EDX) analysis were performed using a ThermoFisher Scientific Titan TEM operated at 300 kV, spot size of 6, camera length of 115 mm, C2 aperture of 70  $\mu\text{m}$ , convergence angle of 25.2 mrad. HR-STEM was collected with a beam current of 0.07 nA and improved by performing drift correction on sequentially acquired STEM images, followed by image averaging. The resulting images were denoised using a LASSO-like soft-thresholding filter to suppress high-frequency noise while preserving structural features. The EDX results show the mass percent distribution maps of individual elements.

**Polarization-Based Electro-Optic Measurement:** Electro-optic measurements were performed using a homebuilt PSCA setup with a 1550 nm HP 81689A continuous-wave laser source and a Nirvana 2017 balanced detector. For absolute intensity measurements, a mechanical chopper was placed in the laser path and modulated at 1.54 kHz for detection with a Stanford SR830 lock-in amplifier. For measuring the modulated transmission intensity, an Agilent 33220A signal generator amplified by a Trek 610C high voltage amplifier was used to apply a 555 Hz sine wave to the sample, with the lock-in amplifier reference signal changed to the function generator reference. The nonlinear electro-optic response was verified by also collecting electro-optic modulation signal at double the frequency of the driving voltage, i.e., at 1110 Hz. Samples were cooled to liquid He temperatures using a Janis 30 continuous flow cryostat system.

The polarization of the probe was set to lie between the ordinary and extraordinary refractive indices, as depicted in Figure 2a. An analyzer placed at the end of the setup was oriented orthogonal to the initial probe polarization state, resulting in no transmission of light through the setup when the sample and compensator were not included. With the sample introduced, the transmission becomes nonzero on account of the birefringence-induced ellipticity. A quarter-wave compensator was then added immediately after the sample to cancel out the native material birefringence with no voltage applied. This returns the transmission of the setup to zero until a voltage is applied to modulate the sample refractive indices and reintroduce ellipticity to the probe.

**Second-Harmonic Generation Polarimetry:** Second-harmonic generation polarimetry experiments were performed using a fundamental wavelength of 800 nm generated by a Spectra-Physics Solstice Ace amplified Ti:Sapphire laser with a 1 kHz repetition rate and 100 fs pulse width. Light was focused onto the sample using a 10 cm focal length lens, producing a 50  $\mu\text{m}$  diameter spot size as determined by knife-edge measurements. Samples were cooled to liquid He temperatures using a Janis 30 continuous flow cryostat system. A bare GdScO<sub>3</sub> substrate of the same type produces no appreciable SHG signal under the same incident power, and thus the SHG signal measured was interpreted as originating entirely from the strained BaTiO<sub>3</sub> film.

**Phase-Field Simulations:** Based on the thermodynamic theory of optical properties, a phase-field model might be formulated, where the thermodynamics of the ferroelectric system was described by its free energy functional,

$$F = \int \left[ f^L(T, P_i^L) + f^e(T, P_i^e) + f^{L-e}(P_i^L, P_i^e) + f^{\text{grad}}(\nabla_i P_j^L) + f^{\text{elas}}(P_i^L, P_i^e, \epsilon_{ij}) + f^{\text{elec}}(P_i^L, P_i^e, E_i) \right] dx^3 \quad (7)$$

where  $P_i^L(x, t)$  is the lattice polarization,  $P_i^e(x, t)$  is the electrical polarization, and  $\sigma_{ij}(x, t)$  is the stress.<sup>[36]</sup>

The evolution of the lattice polarization and electronic polarization is solved separately. The lattice polarization is computed following the relaxational approximation, where relaxational kinetics for the lattice polarization was assumed, and the mechanical displacement, electrical potential,

and electrical polarization instantaneously reach equilibrium, leading to the time-dependent Ginzburg–Landau equation

$$\gamma_{ij}^L \frac{\partial P_j^L}{\partial t} = - \frac{\delta F}{\delta P_i^L} \quad (8)$$

where  $-\frac{\delta F}{\delta P_i^L}$  is the thermodynamic driving force for the temporal evolution of the lattice polarization. The local stress and lattice polarization distribution was used as inputs to the electronic polarization dynamic equation

$$\mu_{ij}^e \frac{\partial^2 P_j^e}{\partial t^2} + \gamma_{ij}^e \frac{\partial P_j^e}{\partial t} = - \frac{\delta F}{\delta P_i^e} \quad (9)$$

where  $-\frac{\delta F}{\delta P_i^e}$  is the thermodynamic driving force for the temporal evolution of the electronic polarization. To compute the local electronic dielectric susceptibility, Equation (7) was solved assuming a small periodic electric field is applied, which yields an analytical solution

$$\tilde{\chi}_{ij}^{e,1}(x_i, \omega) = \left[ B_{ij}^e(x_i) - \epsilon_0 \left( i\omega\gamma_{ij}^e + \omega^2\mu_{ij}^e \right) \right]^{-1} \quad (10)$$

which is related to the curvature of the free-energy landscape with respect to the electronic polarization by,  $B_{ij}^e(x_i) = \epsilon_0 \left( \frac{\partial^2 f}{\partial P_i^e \partial P_j^e} \right)$ . Solving Equation (14) (assuming  $\lambda = 1550$  nm) the local refractive indices might be computed, from the local lattice polarization and stress distribution, thereby naturally including the electro-optic effect and potential piezoelectric effects. As the lattice polarization distribution evolves in response to an applied electric field, the corresponding change to the electronic dielectric susceptibility and the refractive index was computed.

Here  $f^L(P_i^L)$  describes the intrinsic stability of the lattice polarization compared to the high symmetry phase ( $m\bar{3}m$ ) as a Taylor expansion of the polarization about the high symmetry phase, this was equivalent to the Landau free energy density:

$$f^L(T, P_i^L) = f_0 + a_{ij}(T) P_i^L P_j^L + a_{ijkl} P_i^L P_j^L P_k^L P_l^L + a_{ijklmn} P_i^L P_j^L P_k^L P_l^L P_m^L P_n^L + a_{ijklmnop} P_i^L P_j^L P_k^L P_l^L P_m^L P_n^L P_o^L P_p^L \quad (11)$$

where  $a_{ij}$ ,  $a_{ijkl}$ ,  $a_{ijklmn}$ , and  $a_{ijklmnop}$  are the dielectric stiffness coefficients measured under constant stress conditions. For BaTiO<sub>3</sub>, an 8th order expansion was used to describe the stability of the lattice polarization. The thermodynamic coefficients are adapted from ref. [59] to describe the effects of quantum fluctuations at cryogenic temperatures. ref. [60]

The intrinsic free energy density of the electronic polarization, in the absence of the lattice polarization, is described by

$$f^e(T, P_i^e) = \frac{1}{2\epsilon_0} B_{ij}^{e, \text{ref}}(T) P_i^e P_j^e \quad (12)$$

where  $B_{ij}^{e, \text{ref}}(T)$  is related to the refractive index of the equivalent high symmetry phase. The coupling energy density between the lattice and electronic polarization, which determines the electro-optic effect, is given by

$$f^{L-e}(P_i^L, P_i^e) = g_{ijkl}^{LL} P_i^L P_j^L P_k^L P_l^e P_j^e \quad (13)$$

where  $g_{ijkl}^{LL}$  relates the lattice polarization to the refractive index.

The gradient energy density is represented by

$$f^{\text{grad}} = \frac{1}{2} G_{ijkl} \frac{\partial P_i^L}{\partial x_j} \frac{\partial P_k^L}{\partial x_l} \quad (14)$$

where  $G_{ijkl}$  is the gradient energy tensor where the non-zero coefficients are chosen to be  $G_{11} = 0.6$ ,  $G_{22} = -0.6$ , and  $G_{44} = 0.6$ , and the units are normalized by  $\alpha_1 l_0^2$  where  $\alpha_1$  is the first Landau expansion coefficient and  $l_0$  is chosen as 1 nm per grid.

The elastic energy is given by

$$f^{elas} \left( P_i^L, P_i^e, \sigma_{ij} \right) = C_{ijkl} \left( \epsilon_{ij} - \epsilon_{ij}^o \right) \quad (15)$$

where  $C_{ijkl}$  is the elastic stiffness,  $\epsilon_{ij}$  is the total strain, and  $\epsilon_{ij}^o = Q_{ijkl} \sigma_{ij} P_k^L P_l^L + \frac{1}{2\epsilon_0} \pi_{ijkl} \sigma_{ij} P_k^e P_l^e$  is the eigenstrain, where  $Q_{ijkl}$  is the electrostrictive coefficient and  $\pi_{ijkl}$  is the piezo-optic tensor for the high-symmetry phase. The total strain was solved for a thin film boundary condition assuming that the strain relaxes to its equilibrium value at each time step; for simplicity the contribution of the electronic polarization to the eigenstrain was ignored. Further details on solving the elasticity may be found in ref. [61]

The electrostatic energy is given by

$$f^{elec} = -E_i P_i^L - E_i P_i^e - \frac{1}{2} \epsilon_0 \kappa_{ij}^b E_i E_j \quad (16)$$

where  $\epsilon_0$  is the vacuum permittivity and  $\kappa_{ij}^b$  is the background dielectric constant. For simplicity, to compute the evolution of the lattice polarization, only the linear contribution to the electronic polarization was included and added to the background dielectric constant yielding  $f^{elec} = -E_i P_i^L - \frac{1}{2} \epsilon_0 \kappa_{ij}^b E_i E_j$ , where  $\kappa_{ij}^b = 10$  and is isotropic. Here  $\kappa_{ij}^b$  contains contributions from the electronic contribution and the vacuum and other hard modes. Appendix A and Table S5 (Supporting Information) contain all coefficients used in the phase-field simulations.

For the simulations, a system size of  $128 \Delta x_1 \times 128 \Delta x_2 \times 56 \Delta x_3$  was used. There were 12  $\Delta x_3$  grid points for the substrates where the elastic constants were assumed to be the same as the ferroelectric film, and there are 4  $\Delta x_3$  grid points acting as an air layer above the film. The thickness of BaTiO<sub>3</sub> was set to be  $40\Delta x_3$ . Periodic boundary conditions were used along the in-plane lateral directions, and natural boundary conditions were used along the film-substrate and film-air interfaces. The interface between the film and the substrate was assumed to be coherent, and hence the misfit strain was calculated using the equivalent cubic lattice parameters for BaTiO<sub>3</sub> and the pseudocubic lattice parameters for GdScO<sub>3</sub>.<sup>[62]</sup>

$$\epsilon_{11} = \frac{a_{GdScO_3}^{[110]_o} - a_{BaTiO_3}^{eq}}{a_{BaTiO_3}^{eq}}, \epsilon_{22} = \frac{a_{GdScO_3}^{[001]_o} - a_{BaTiO_3}^{eq}}{a_{BaTiO_3}^{eq}}, \epsilon_{12} = \epsilon_{21} = 0 \quad (17)$$

where the lattice parameters for BaTiO<sub>3</sub> are  $a_{BaTiO_3}^{eq} = 4.01 \text{ \AA} (1 + 1.15 \times 10^{-5} (T - 300 \text{ K}))$  and  $a_{GdScO_3}^{[110]_o} = 3.970 \text{ \AA} (1 + 1.09 \times 10^{-5} (T - 300 \text{ K}))$  and  $a_{GdScO_3}^{[001]_o} = 3.966 \text{ \AA} (1 + 1.09 \times 10^{-5} (T - 300 \text{ K}))$ .

The simulations begin with an initial condition of  $P_i^L(x_i, t = 0) = [0.0 \ 0.0 \ 0.1 \ \text{C m}^{-2}] + \Delta P^{noise}(x_i, t = 0)$ , where  $|P^{noise}| = 0.1 \ \text{C m}^{-2}$ . To simulate the evolution of the polarization under an applied electric field and the corresponding electro-optic effect, a uniform electric field was applied along the [100] direction ranging from  $-70$  to  $70 \ \text{kV cm}^{-1}$ . The electric field was incremented by  $0.7 \ \text{kV cm}^{-1}$  every 100 timesteps. The linear electro-optic effect and quadratic electro-optic effect were found by taking the average of the refractive index over the ferroelectric material as a function of an applied electric field and fitting to a polynomial expansion centered around zero. The simulations for the evolution of the lattice polarization were completed using the mu-Pro software.

**Synchrotron-Based Reciprocal Space Mapping:** Synchrotron X-ray diffraction experiments were performed at the ID4B (QM2) beamline at the Cornell high energy synchrotron source (CHESS). The incident X-ray energy was 20 keV. An area detector array (Pilatus 6M) was used to collect the scattering intensities in a grazing incidence reflection geometry ( $8^\circ$  incidence angle). The sample was rotated through  $360^\circ$  rotations, sliced

into  $0.1^\circ$  frames. Geometric parameters of the Pilatus 6M detector, such as detector distance, tilting, rotation, and direct beam position, were extracted using a standard CeO<sub>2</sub> powder reference.

## Supporting Information

Supporting Information is available from the Wiley Online Library or from the author.

## Acknowledgements

A.S., S.H., and A.R. contributed equally to this work. This work was primarily supported through DOE-BES, under award No. DE-SC0012375. S.H., V.A.S., and V.G. acknowledge support from DOE-BES grant DE-SC0012375 for partial electro-optic measurements, partial SHG measurements, X-ray experiments, and manuscript preparation. A.S. and V.G. acknowledge support from the Center for 3D Ferroelectric Microelectronics and Manufacturing (3DFeM<sub>2</sub>), an Energy Frontier Research Center funded by the U.S. Department of Energy, Office of Science, Office of Basic Energy Sciences Energy Frontier Research Centers program under Award Number DE-SC0021118, for partial electro-optic measurements, partial SHG measurements, optical characterization, and manuscript preparation. I.R.P. and B.B. acknowledge the National Science Foundation DMREF Grant No. DMR-2522897 for partial electro-optic and spectroscopic ellipsometry measurements. S.S. and V.G. acknowledge support from the National Science Foundation supported Penn State MRSEC for Nanoscale Science Grant Number DMR-2011839 for UV-vis spectroscopy measurements. A.R., L.Q.C., and V.G. acknowledge support from the U.S. Department of Energy, Office of Science, Office of Basic Energy Sciences, under Contract No. DE-SC0020145 for the phase-field simulations and manuscript preparation. A.R. also acknowledges the support of the National Science Foundation Graduate Research Fellowship Program under Grant No. DGE1255832. The phase-field simulations in this work were performed using Bridges-2 at the Pittsburgh Supercomputing Center through allocation MAT230041 from the ACCESS program, which is supported by National Science Foundation Grants Nos. 2138259, 2138286, 2138307, 2137603 and 2138296. The BaTiO<sub>3</sub> thin films were synthesized at the Platform for the Accelerated Realization, Analysis, and Discovery of Interface Materials (PARADIM), which is supported by the National Science Foundation (NSF) under Cooperative Agreement No. DMR-2039380. D.S. and D.G.S. acknowledge support from the NSF through PARADIM under Cooperative Agreement No. DMR-2039380. This work is based on research conducted at the Center for High-Energy X-ray Sciences (CHEXS), which is supported by the National Science Foundation (BIO, ENG and MPS Directorates) under award DMR-2342336. This research used Electron Microscopy resources of the Center for Functional Nanomaterials (CFN), which is a U.S. Department of Energy Office of Science User Facility, at Brookhaven National Laboratory under Contract No. DE-SC0012704.

## Conflict of Interest

The authors have a provisional patent filed on this work. Long-Qing Chen has a financial interest in MuPRO, LLC, a company which licenses and markets the software package used in this research.

## Data Availability Statement

The data that supports the findings of this study are available within the article. Datasets used for the generation of figures presented in the article is available at <https://doi.org/10.5281/zenodo.17296490>. Additional data related to the film growth and structural characterization is available at <https://doi.org/10.34863/k6vg-fr77>. Any additional data connected to the study are available from the corresponding author upon reasonable request.

## Keywords

barium titanate, electro-optic effect, phase-field method, pockels effect, strain-tuning

Received: April 21, 2025

Revised: September 22, 2025

Published online: October 11, 2025

- [1] A. Yariv, P. Yeh *Optical Waves in Crystals: Propagation, and Control of Laser Radiation*, John Wiley & Sons (Wiley-Interscience), New York, **2002**.
- [2] R. W. Boyd, *Nonlinear Optics*, Elsevier, San Diego, California, **2003**, <https://doi.org/10.1016/B978-0-12-121682-5.X5000-7>.
- [3] C. Chen, G. Liu, *Annu. Rev. Mater. Res.* **1986**, *16*, 203.
- [4] C. Javerzac-Galy, K. Plekhanov, N. R. Bernier, L. D. Toth, A. K. Feofanov, T. J. Kippenberg, *Phys. Rev. A* **2016**, *94*, 053815.
- [5] N. J. Lambert, A. Rueda, F. Sedlmeir, H. G. L. Schwefel, *Adv. Quantum Technol.* **2020**, *3*, 1900077.
- [6] M. Kjaergaard, M. E. Schwartz, J. Braumüller, P. Krantz, J. I. Wang, S. Gustavsson, W. D. Oliver, *Annu. Rev. Condens. Matter Phys.* **2020**, *11*, 369.
- [7] C. D. Bruzewicz, J. Chiaverini, R. McConnell, J. M. Sage, *Appl. Phys. Rev.* **2019**, *6*, 021314.
- [8] B. Lekitsch, S. Weidt, A. G. Fowler, K. Mølmer, S. J. Devitt, C. Wunderlich, W. K. Hensinger, *Sci. Adv.* **2017**, *3*, 1601540.
- [9] J. C. Bardin, D. H. Slichter, D. J. Reilly, *IEEE J. Microwaves* **2021**, *1*, 403.
- [10] P. Pintus, M. Soltani, G. Moody, *Nat. Photonics* **2024**, *18*, 306.
- [11] P. Pintus, A. Singh, W. Xie, L. Ranzani, M. V. Gustafsson, M. A. Tran, C. Xiang, J. Peters, J. E. Bowers, M. Soltani, *Optica* **2022**, *9*, 1176.
- [12] A. W. Elshaari, W. Pernice, K. Srinivasan, O. Benson, V. Zwiller, *Nat. Photonics* **2020**, *14*, 285.
- [13] A. A. Demkov, C. Bajaj, J. G. Ekerdt, C. J. Palmstrøm, S. J. Ben Yoo, *J. Appl. Phys.* **2021**, *130*, 070907.
- [14] F. Eltes, G. E. Villarreal-Garcia, D. Caimi, H. Siegwart, A. A. Gentile, A. Hart, P. Stark, G. D. Marshall, M. G. Thompson, J. Barreto, J. Fompeyrine, S. Abel, *Nat. Mater.* **2020**, *19*, 1164.
- [15] S. Abel, F. Eltes, J. E. Ortmann, A. Messner, P. Castera, T. Wagner, D. Urbonas, A. Rosa, A. M. Gutierrez, D. Tulli, P. Ma, B. Baeuerle, A. Josten, W. Heni, D. Caimi, L. Czornomaz, A. A. Demkov, J. Leuthold, P. Sanchis, J. Fompeyrine, *Nat. Mater.* **2019**, *18*, 42.
- [16] S. Kazaoui, J. Ravez, C. Elissalde, M. Maglione, *Ferroelectrics* **1992**, *135*, 85.
- [17] V. Bovtun, D. Nuzhnyy, M. Kempa, T. Ostapchuk, V. Skoromets, J. Suchanicz, P. Czaja, J. Petzelt, S. Kamba, *Phys. Rev. Mater.* **2021**, *5*, 14404.
- [18] A. Rosa, D. Tulli, P. Castera, A. M. Gutierrez, A. Griol, M. Baquero, B. Vilquin, F. Eltes, S. Abel, J. Fompeyrine, P. Sanchis, *Opt. Mater. Express* **2017**, *7*, 4328.
- [19] T. Tsurumi, J. Li, T. Hoshina, H. Kakemoto, M. Nakada, J. Akedo, *Appl. Phys. Lett.* **2007**, *91*, 182905.
- [20] T. Hamano, D. J. Towner, B. W. Wessels, *Appl. Phys. Lett.* **2003**, *83*, 5274.
- [21] K. Laabidi, M. D. Fontana, M. Maglione, B. Jannot, K. A. Müller, *Europhys. Lett.* **1994**, *16*, 309.
- [22] M. P. McNeal, S.-J. Jang, R. E. Newnham, *J. Appl. Phys.* **1998**, *83*, 3288.
- [23] D. Chelladurai, M. Kohli, J. Winiger, D. Moor, A. Messner, Y. Fedoryshyn, M. Eleraky, Y. Liu, H. Wang, J. Leuthold, *Nat. Mater.* **2025**, *24*, 868.
- [24] R. Guo, L. E. Cross, S.-E. Park, B. Noheda, D. E. Cox, G. Shirane, *Phys. Rev. Lett.* **2020**, *84*, 5423.
- [25] B. Noheda, D. E. Cox, *Phase Transitions* **2006**, *79*, 5.
- [26] H. Fu, R. E. Cohen, *Nature* **2020**, *403*, 281.
- [27] D. Viehland, *J. Am. Ceram. Soc.* **2006**, *89*, 775.
- [28] R. E. Newnham, *MRS Bull.* **1997**, *22*, 20.
- [29] T. T. A. Lummen, Y. Gu, J. Wang, S. Lei, F. Xue, A. Kumar, A. T. Barnes, E. Barnes, S. Denev, A. Belianinov, M. Holt, A. N. Morozovska, S. V. Kalinin, L. Q. Chen, V. Gopalan, *Nat. Commun.* **2014**, *5*, 3172.
- [30] M. Zgonik, P. Bernasconi, M. Duelli, R. Schlessler, P. Günter, M. H. Garrett, D. Rytz, Y. Zhu, X. Wu, *Phys. Rev. B* **1994**, *50*, 5941.
- [31] W. Guo, A. B. Posadas, A. A. Demkov, *J. Vacuum Sci. Technol. A* **2021**, *39*, 030804.
- [32] P. Tang, D. J. Towner, T. Hamano, A. L. Meier, B. W. Wessels, *Opt. Express* **2004**, *12*, 5962.
- [33] M. Adachi, Y. Akishige, T. Asahi, K. Deguchi, K. Gesi, K. Hasebe, T. Hikita, T. Ikeda, Y. Iwata, M. Komukae, T. Mitsui, E. Nakamura, N. Nakatani, M. Okuyama, T. Osaka, A. Sakai, E. Sawaguchi, Y. Shiozaki, T. Takenaka, K. Toyoda, T. Tsukamoto, T. Yagi, *BaTiO<sub>3</sub> (cubic) [F] Survey, 1A-10: Datasheet from Landolt-Börnstein – Group III Condensed Matter · Volume 36A1: ‘Oxides’ in SpringerMaterials*, (Eds.: Y. Shiozaki, E. Nakamura, T. Mitsui), Springer-Verlag, Berlin Heidelberg, **2001**, <https://doi.org/10.1007/b53034>.
- [34] C. J. Johnson, *Appl. Phys. Lett.* **1965**, *7*, 221.
- [35] D. Vanderbilt, M. H. Cohen, *Phys. Rev. B* **2001**, *63*, 94108.
- [36] A. Ross, M. S. M. Ali, A. Saha, R. Zu, V. Gopalan, I. Dabo, L.-Q. Chen, *Phys. Rev. B* **2025**, *111*, 085109.
- [37] M. Aillerie, N. Théofanous, M. D. Fontana, *Appl. Phys. B: Lasers Opt.* **2000**, *70*, 317.
- [38] X. Yuan, T. Yamada, L. Meng, *Appl. Phys. Lett.* **2022**, *121*, 152903.
- [39] M. Reynaud, H. Huyen, C. Du, W. Li, A. B. Posadas, X. Pan, A. A. Demkov, *ACS Appl. Electron. Mater.* **2023**, *5*, 4605.
- [40] H. Yu, N. Guo, C. Deng, H. Han, W. Li, C. Lebudu, S. Wang, Y. Li, Y. Chen, S. Peng, J. Zhang, J. Ma, Q. Zheng, J.-F. Li, Q. Li, *Adv. Funct. Mater.* **2024**, *34*, 2315579.
- [41] K. J. Kormondy, S. Abel, F. Fallegger, Y. Popoff, P. Ponath, A. B. Posadas, M. Sousa, D. Caimi, H. Siegwart, E. Uccelli, L. Czornomaz, C. Marchiori, J. Fompeyrine, A. A. Demkov, *Microelectron. Eng.* **2015**, *147*, 215.
- [42] Y. Cao, Y. Wen, Y. Yang, F. Zhang, W. Zhang, J. Du, Y. Zhang, Z. Wu, J. Wu, *Appl. Phys. Lett.* **2025**, *126*, 111104.
- [43] Y. Wen, Y. Cao, H. Chen, X. Du, J. Guo, J. Shen, F. Zhang, T. Bian, Y. An, H. Ren, Z. Wu, W. Liu, Y. Zhang, *Adv. Opt. Mater.* **2024**, *12*, 2303058.
- [44] M.-J. Sun, C. Zheng, Y. Gao, A. Johnston, A. M. Najarian, P.-X. Wang, O. Voznyy, S. Hoogland, E. H. Sargent, *Adv. Mater.* **2021**, *33*, 2006368.
- [45] Y. Gao, G. Walters, Y. Qin, B. Chen, Y. Min, A. Seiftokaldani, B. Sun, P. Todorovic, M. I. Saidaminov, A. Lough, S. Tongay, S. Hoogland, E. H. Sargent, *Adv. Mater.* **2019**, *31*, 1808336.
- [46] S. Kondo, T. Yamada, A. K. Tagantsev, P. Ma, J. Leuthold, P. Martelli, P. Boffi, M. Martinelli, M. Yoshino, T. Nagasaki, *Appl. Phys. Lett.* **2019**, *115*, 092901.
- [47] S. Kondo, R. Shimura, T. Teranishi, A. Kishimoto, T. Nagasaki, H. Funakubo, T. Yamada, *Jpn. J. Appl. Phys.* **2021**, *60*, 070905.
- [48] M. Zhu, Z. Du, S. S. Chng, S. H. Tsang, E. H. T. Teo, *J. Mater. Chem. C* **2018**, *6*, 12919.
- [49] Y. Wen, H. Ren, X. Du, Y. Zhang, *J. Appl. Phys.* **2024**, *136*, 113103.
- [50] X. Yuan, Y. Sakurai, S. Kondo, M. Yoshino, T. Nagasaki, T. Yamada, *Jpn. J. Appl. Phys.* **2022**, *61*, SN1005.
- [51] S. Gupta, A. Paliwal, R. Guo, A. S. Bhalla, V. Gupta, M. Tomar, *Optical Materials* **2018**, *85*, 26.
- [52] A. Dastgir, X. Yuan, Y. Shen, D. Kan, Y. Shimakawa, H. Sawaki, S. Kondo, T. Yamada, *Appl. Phys. Lett.* **2025**, *126*, 242901.
- [53] W. Pabst, S. Hřibálová, *J. Eur. Ceram. Soc.* **2021**, *41*, 2058.
- [54] Z. Xiong, J. Zhu, J. Ma, K. Zhang, Y. Zhang, J. Liu, *Appl. Phys. Lett.* **2025**, *126*, 191901.
- [55] A. R. Johnston, *J. Appl. Phys.* **1971**, *42*, 3501.

- [56] L. B. Kong, S. Li, T. S. Zhang, J. W. Zhai, F. Y. C. Boey, J. Ma, *Progress Mater. Sci.* **2010**, *55*, 840.
- [57] S. A. Denev, T. T. A. Lummen, E. Barnes, A. Kumar, V. Gopalan, *J. Am. Ceram. Soc.* **2011**, *94*, 2699.
- [58] S. Hazra, T. Schwaigert, A. Ross, H. Lu, U. Saha, V. Trinquet, B. Akkopru-Akgun, B. Z. Gregory, A. Mangu, S. Sarker, T. Kuznetsova, S. Sarker, X. Li, M. R. Barone, X. Xu, J. W. Freeland, R. Engel-Herbert, A. M. Lindenberg, A. Singer, S. Trolier-McKinstry, D. A. Muller, G.-M. Rignanese, S. Salmani-Rezaie, V. A. Stoica, A. Gruverman, L.-Q. Chen, D. G. Schlom, V. Gopalan, *Adv. Mater.* **2024**, *36*, 2408664.
- [59] Y. L. Li, L. E. Cross, L. Q. Chen, *J. Appl. Phys.* **2005**, *98*, 064101.
- [60] J. H. Barrett, *Phys. Rev.* **1952**, *86*, 118.
- [61] Y. L. Li, S. Y. Hu, Z. K. Liu, L. Q. Chen, *Acta Mater.* **2002**, *50*, 395.
- [62] R. Uecker, B. Velickov, D. Klimm, R. Bertram, M. Bernhagen, M. Rabe, M. Albrecht, R. Fornari, D. G. Schlom, *J. Cryst. Growth* **2008**, *310*, 2649.